The paper was published in the proceedings of the 20th International Conference on Soil Mechanics and Geotechnical Engineering and was edited by Mizanur Rahman and Mark Jaksa. The conference was held from May 1st to May 5th 2022 in Sydney, Australia.

Proceedings of the 20th International Conference on Soil Mechanics and Geotechnical Engineering– Rahman and Jaksa (Eds)
© 2022 Australian Geomechanics Society, Sydney, Australia, ISBN 978-0-9946261-4-1

Shear band measurement in transparent sand

Mesure de la bande de cisaillement dans un sable transparent

David H Marx & Jorge G Zornberg
Department of Civil, Architectural and Environmental engineering, The University of Texas at Austin, United States of America, dawie.marx@utexas.edu

ABSTRACT: Shear band development in a lubricated triaxial specimen was studied using a transparent sand. The transparent, granular, soil surrogate was manufactured by saturating fused quartz with a mineral oil mix with a matching refractive index. Displacement across a laser illuminated section of the specimen was analysed using digital image analysis techniques. By calculating the second order central moments of the incremental shear strain distributions the inclination of the shear concentration, and the anisotropy of the strain field, could be measured. The development of the shear band inclination and stress-induced anisotropy with increasing axial strain was correlated to the stress-strain behaviour of the specimen. This includes strain localization in the specimen which was found to coincide with the onset of dilation. In addition, the onset of plastic deformation corresponded with large oscillations in the shear band inclination, representative of the bulging-type failure.

RÉSUMÉ: Le développement de la bande de cisaillement dans un échantillon triaxial lubrifié a été étudié en utilisant des sables transparents. Le sol granulaire transparent a été conçu en saturant du verre de quartz avec d'huile minérale qui égalise leur indice de réfraction. Le déplacement à travers une section éclairée par laser dans l'échantillon a été analysé en utilisant des techniques d'analyse d'images numériques. En calculant les moments centraux du second ordre des distributions incrémentielles de déformation de cisaillement, l'inclinaison de la concentration de cisaillement et l'anisotropie du champ de déformation ont pu être mesurées. Le développement de l'inclinaison de la bande de cisaillement et la contrainte anisotrope a été corrélé au comportement contrainte-déformation de l'échantillon. Cela inclut la localisation de la déformation dans l'échantillon qui coïncide avec le début de la dilatation. De plus, le début de la déformation plastique correspond à des grandes oscillations sur l'inclinaison de la bande de cisaillement, représentatives de la rupture type bombage..

KEYWORDS: shear bands, transparent soil, fused quartz, digital image correlation

1 INTRODUCTION

The study of failure mechanisms is key to geotechnical engineering. If the plastic deformation that the soil will experience under the applied loads is understood, the engineer can design the structure to be stable. Plastic deformation in soil is typically limited to narrow zones of localized strain, also known as shear bands.

The quantification of shear bands is of particular importance in soil-structure interaction problems such as geogrid reinforcement applications. By measuring the shear bands that form while the geogrid interacts with the soil, the load-transfer mechanism can be better understood (consider the work of Dyer, 1985). Once the mechanism is defined the geogrid reinforcement can be optimized to enhance load transfer.

Before investigating the effect of reinforcement on shear band development, it is prudent to establish a baseline of the soil behaviour by considering unreinforced samples. For this research, the development of shear bands was investigated using an unreinforced triaxial specimen of transparent sand. Two measures of the shear strain concentration, its inclination and anisotropy, were evaluated and used to quantify the shear band development as the test progressed.

1.1 Shear band measurement in element tests

Experimental measurement of shear bands requires a view inside the sample or model. This is typically only possible in lab scale experiments such as centrifuge models, or specialized element testing.

Previous research has focused on shear band formation in element tests. For example, Scrapelli & Wood (1982) x-rayed samples filled with lead shot in direct shear tests. Vardoulakis (1980), Le Bouil et al. (2014), Nguyen & Amon (2016), and Rechenmacher & Finno (2020) studied different versions of biaxial tests on glass beads or sand samples. The state of the art of shear band measurement in element tests is microtomography scans of triaxial samples, such as those done by Hall et al. (2010) and Takano et al. (2015).

All three of the testing approaches mentioned have physical constraints that limit the interpretation of the results to certain conditions. For example, two-dimensional setups, such as the biaxial test, are limited to plane strain testing. In addition, the transparent windows that have been used to observe the sample may induce friction. Samples imaged with microtomography are limited either in size or resolution due to the high attenuation of soil particles.

1.2 Transparent soils

To address the shortcomings of 2D experiments and small 3D experiments, transparent soil can be used as a soil surrogate. Various families of fine-grained and coarse-grained transparent soils have been developed over the years (Iskander et al. 2015). Tests on coarse-grained specimens can be conducted using fused quartz saturated with a blend of clear mineral oils. By matching the refractive indices of the two materials light passes through the mixture, rather than refracting. Thus, the mixture is transparent.

A perfect match between the refractive index of the quartz and the oils is challenging. A benefit of the inevitable mismatch is that when a sheet laser is shined into the sample the edges of the particles along the plane refract the laser. Consequently, these edges become illuminated and can be tracked with a digital camera as the soil sample deforms. Thus, the displacement of grains inside the sample can be measured and shear bands can consequently be tracked (Peng & Zornberg 2019).

While overcoming some of the limitations of biaxial experiments and microtomography scans, oil-saturated fused quartz has limitations of its own. For example, oil-saturated samples tend to amplify slip-stick behaviour during shear. However, these tests do offer a unique view into the development of shear bands in triaxial samples.

2 EXPERIMENTAL METHODOLOGY

2.1 Transparent sand

The transparent sand adopted in this study was manufactured by index matching fused quarts with a mixture of two oils: 52% Puretol 7 Special and 48% Paraflex HT4, both manufactured by Petro-Canada. The particle size distribution of the material is shown in Figure 1. The coefficient of uniformity is 2.8 and the coefficient of curvature is 1.4. Thus, the material classifies as a Poorly Graded Sand (SP) according to the Unified Soil Classification System. Minimum and maximum void ratios of 0.52 and 0.72, respectively, were measured.

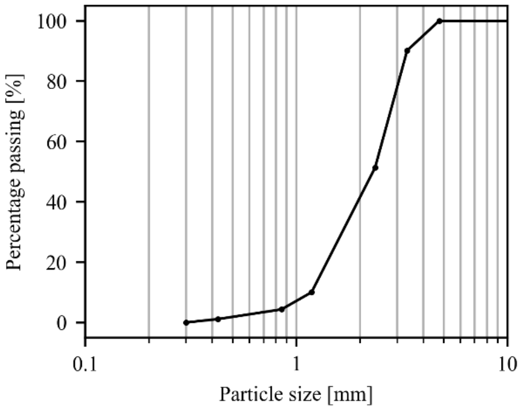

Figure 1. Particle size distribution of the fused quartz used in this study.

2.2 Triaxial setup and testing

A 50 mm diameter, 100 mm tall sample was prepared in a triaxial setup with lubricated, enlarged platens. Two silicone discs lubricated with thin layers of vacuum grease were used at both platens. A custom-made, transparent silicone membrane was used for the test as conventional latex membranes are neither transparent nor compatible with oil. The oil was used both to saturate the sample and as a confining liquid. Two flow pumps connected to bladder accumulators were used to measure volume changes in the specimen. The repeatability of the oil saturated, fused quartz samples tested with the custom membranes is adequate as discussed by Marx & Zornberg (2020).

A slice through the sample was illuminated with a 450 mW laser with a wavelength of 638 nm. Images of this section were captured with a Canon EOS 5DS R camera fitted with a Sigma 50 mm f/1.4 lens at a rate of 10 images/minute. This is equivalent to one image approximately every 0.02% axial strain. A simplified diagram of the experimental setup is shown in Figure 2.

The specimen described in this paper was tested under an effective confining stress of 100 kPa after back pressure saturation to approximately 300 kPa. The B-value was 0.99 and no air-bubbles were observed in the sample. The triaxial compression test was displacement-controlled, conducted at an axial strain rate of 6%/hour. The comparatively slow displacement rate was dictated by the interval at which images were collected for the digital image correlation. In addition, the slow strain rate ensured that the pore pressure could sufficiently dissipate through the lubricated ends.

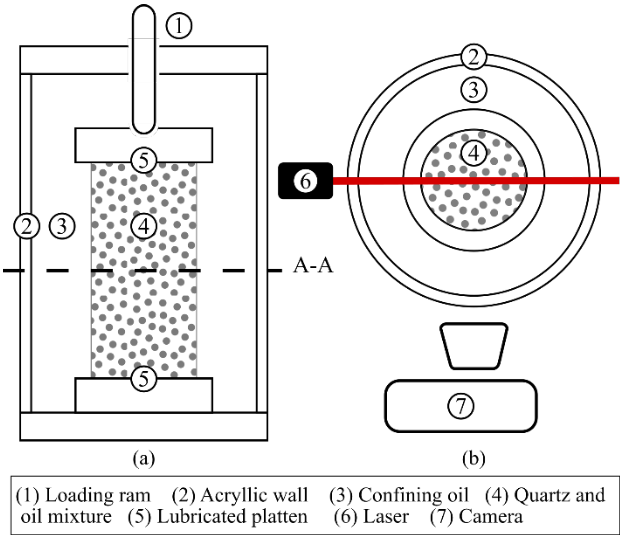

Figure 2. Simplified diagram of experimental setup: (a) Elevation along the laser plane; (b) Plan view (Section A-A).

3 IMAGE ANALYSIS

3.1 Image pre-processing

The images were captured in RAW format, subsequently demosaiced and finally converted to greyscale. Air bubbles, particle edges and small particles refract comparatively more light than the typical particle. This results in bright spots in the image. Consequently, the greyscale image was first transformed to a natural logarithmic scale to improve the contrast of the darker particles.

As the particles in the sample move during shear the light refracted by a given particle changes. Consequently, the illumination across the sample is constantly varying. At large strain levels the change in illumination may be significant enough to result in failure of some digital image correlation algorithms. Consequently, the exposure of the images was first normalized using the contrast limited adaptive histogram equalization (CLAHE) algorithm implemented in `scikit-image` (Van der Walt et al 2014). Some variation in image-to-image exposure remained after equalization, as too severe equalization results in overexposure of the particle edges.

The OpenCV software package (Bradski 2000) was used to correct the images for various types of distortion. Lens distortion was corrected by firstly capturing images of dots on a regular grid from different angles to calculate the intrinsic camera matrix and the distortion coefficients (refer to function `calibrateCamera()`). Subsequently, the matrix and the coefficients were used to correct the images for lens distortion (refer to function: `undistort()`).

Once the images were corrected for lens distortion, they were aligned to compensate for minute camera movements during the test. LEDs on a fixed frame were used as reference points. For each image a homography matrix was calculated between the coordinates of the LED's in the reference image and their respective coordinates in the image under consideration (refer to function `findHomography()`). Subsequently, all images were transformed such that the coordinates of the LED's align to the first image (refer to function `warpPerspective()`)

A similar approach was followed to correct the images for distortion by the cell wall. First, a homography matrix was calculated from the real coordinates and distorted image coordinates for a series of reference points on the sample. Next, this matrix was used to undistort the images. For further discussion image distortion and Digital Image Correlation refer to White et al. (2003).

3.2 Digital Image Correlation

Digital image correlation (DIC) is an optical technique used to measure full field deformation and motion of a target surface (Schreier et al. 2009). Firstly, a series of images are recorded of a target pattern. For geotechnical problems the pattern is typically the soil itself. In this study the target pattern is the illuminated edges of the quartz particles on the laser plane. Next, for the "local" DIC method subsets (or patches) of the pattern are extracted from a reference image and matched with subsequent target images. Since the locations of the subsets are known in both the reference and the target image, the displacement of the subset can be calculated. This process is repeated across the sample to generate a displacement field. Subsequently, strain fields can be calculated using the measured displacement fields.

For this analysis the GeoPIV-RG software by Stanier et al. (2016) was used. Jones & Iadicola (2018) recommend that the subsets be large enough to contain at least three DIC pattern features. The largest particles in these images are approximately 75 px across. The particle size, as well as the inconsistent image exposure, necessitated the use of comparatively large, 256 px-diameter patches (the sample is approximately 900 px across). However, these large patches were spaced closely (64 px) to increase the measurement resolution.

3.3 Shear band analysis

Incremental shear strain fields of the section through the sample are shown in Figure 3 for increasing values of axial strain. Incremental strains, rather than cumulative strains, were analysed to facilitate interpretation due to the large number of unique shear strain concentrations (Scrapelli & Wood 1982). The incremental strain shown in Figure 3 corresponds to the shear strain occurring over a 0.06% increment of axial strain. For example, the shear strain that developed when the axial strain increased from 0.44% to 0.5% is shown in Figure 3a. In some of the plots a well-defined shear band is visible (e.g., Figure 3d) while for other plots the strain field is reasonably uniform (e.g., Figure 3b).

The the shear strain localizations was quantified following the approach reported by Nguyen & Amon (2016). The shear bands are described in terms of the eigenvalues and eigenvectors of the covariance matrix of the incremental shear strain distribution. The covariance matrix is defined as:

$$cov[I(x,y)] = \begin{bmatrix} \mu_{20}/\mu_{00} & \mu_{11}/\mu_{00} \\ \mu_{11}/\mu_{00} & \mu_{02}/\mu_{00} \end{bmatrix} \quad (1)$$

where $I(x,y)$ is the incremental shear strain at location (x,y) on the image, and $\mu_{00}, \mu_{11}, \mu_{20}, \mu_{02}$ are the central moments of the incremental shear strain distribution, calculated as (Szeliski 2010):

$$\mu_{pq} = \sum_x \sum_y (x - \bar{x})^p (y - \bar{y})^q I(x,y) dxdy \quad (2)$$

where $p + q$ is the order of the moment μ_{pq} ; x, y coordinates of the strain field, and $\bar{x}, \bar{y}$ coordinates of the centroid.

Were this a plate of varying thickness, rather than a distribution of incremental shear strain, the eigenvectors of the covariance matrix of the thickness would have pointed in the directions of the principal axes of rotation of the plate. Thus, the axes around which the plate can spin stably (i.e. the directions for which the angular momentum and angular velocity coincide).

The eigenvector associated with the largest eigenvalue of the covariance matrix of the shear strain distributions shown in Figure 3, points in the direction of the maximum variability in the shear strain field. That is, the direction of strain localization. Due to the noise in the strain fields the distributions were first raised to the third power as a high-pass filter before calculating the covariance matrix.

For each of the strain fields the inclination of the strain localization relative to the vertical axis (θ) was calculated (i.t.o. the second and third quadrant, see schematic in Figure 3k).

Furthermore, the ratio of the two eigenvalues is an indication of the spatial variability of the data, i.e., the anisotropy in the incremental shear strain distribution. The anisotropy (A) is defined as:

$$A = 1 - \lambda_2/\lambda_1 \quad (3)$$

where λ_2 is the smallest eigenvalue of the covariance matrix and λ_1 is the largest eigenvalue.

Anisotropy, $A = 0$ represents an isotropic strain field, while comparatively large values of A correspond to high degrees of anisotropy that are characteristic of strain localization.

4 RESULTS

4.1 Stress-strain behaviour

Figure 4 shows the deviatoric stress and volumetric strain measured during triaxial testing for increasing axial strains. The deviatoric stresses increases smoothly until reaching a yield value at approximately 1.5% axial strain. The maximum shear stress (peak) corresponds to approximately 9% axial strain, beyond which the response shows a comparatively gradual shear strength loss. Thus, there is no distinct strain softening. This corresponds to the post yield bulging observed in the sample, and the continued dilation of the sample at high axial strain levels. Hettler & Vardoulakis (1984) found that diffuse bulging occurred for when lubricated platens were used. The peak, secant friction angle of this single specimen (ϕ') is 44° and the angle of dilation (ψ) is 24°.

A feature that has been reported in tests involving fused quartz saturated with oil is the so-called "slip-stick" behaviour (or load oscillations) that can be observed after yielding (Ezzein & Bathurst 2011). Load bearing particle chains form, collapse, and then reform during post-yield shearing. These slip-stick events are irreversible and correspond to plastic deformation. The recurrence interval and magnitude of the slip events increases with confining stress (Gao et al. 2018) and increased lubrication (Galaz et al 2018). The lubrication reduces the number of force chains in the sample such that buckling of any one of them has a significant effect on the measured deviatoric stress. In addition, tests conducted at comparatively low displacement rate also show increased magnitude of the slip events (Ozbay & Cabalar 2016). The sampling rate of the loadcell, pressure transducers and linear variable differential transformers of 1Hz was sufficient to measure the slip stick behaviour. However, the resolution of the DIC strain field measurements was unfortunately too coarse to capture this behaviour.

4.2 Shear strain inclination and anisotropy

The shear band inclination (θ) and shear strain anisotropy (A) measured during testing is shown in Figure 4 for increasing values of axial strain. As mentioned, and consistent with the results presented in Figure 3, the incremental shear strain values shown in Figure 4 were also calculated over 0.06% axial strain increments. Polynomial lines of best fit are indicated on the θ-curve for the two series of conjugated shear planes that formed to better illustrate the trend in the data.

The two metrics, inclination and anisotropy, should be interpreted with the understanding that the images analysed were collected from a two-dimensional cross-section of a three-dimensional system.

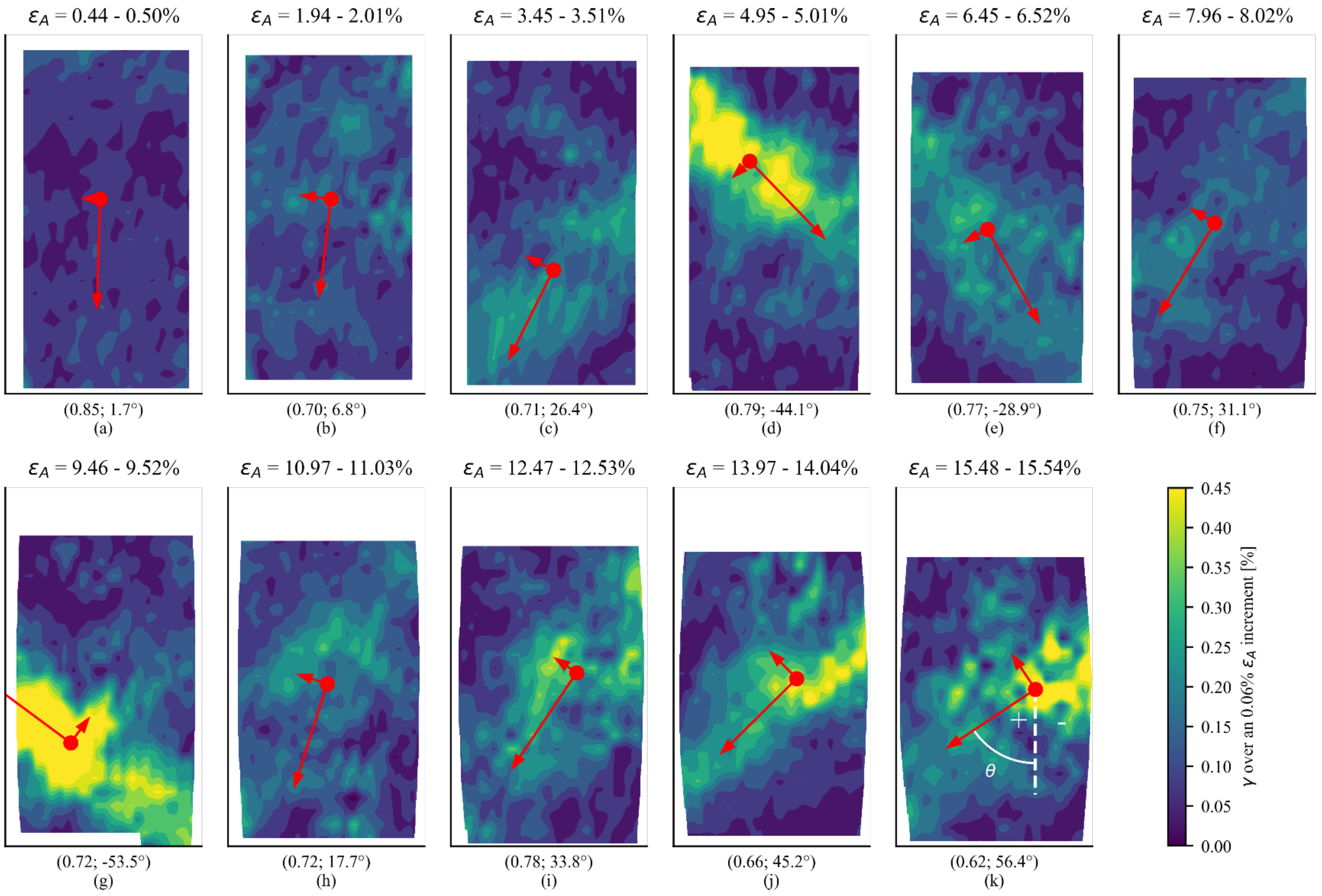

Figure 3. Incremental shear strain distribution (γ) for increasing values of axial strain (ε_A). The changes in shear strain are shown for increments of 0.06% axial strain. The arrows represent the directions of the major and minor axis of incremental shear strain and originate from the centroid of the distribution. For each plot the stress anisotropy and inclination of the shear band are indicated (A, θ).

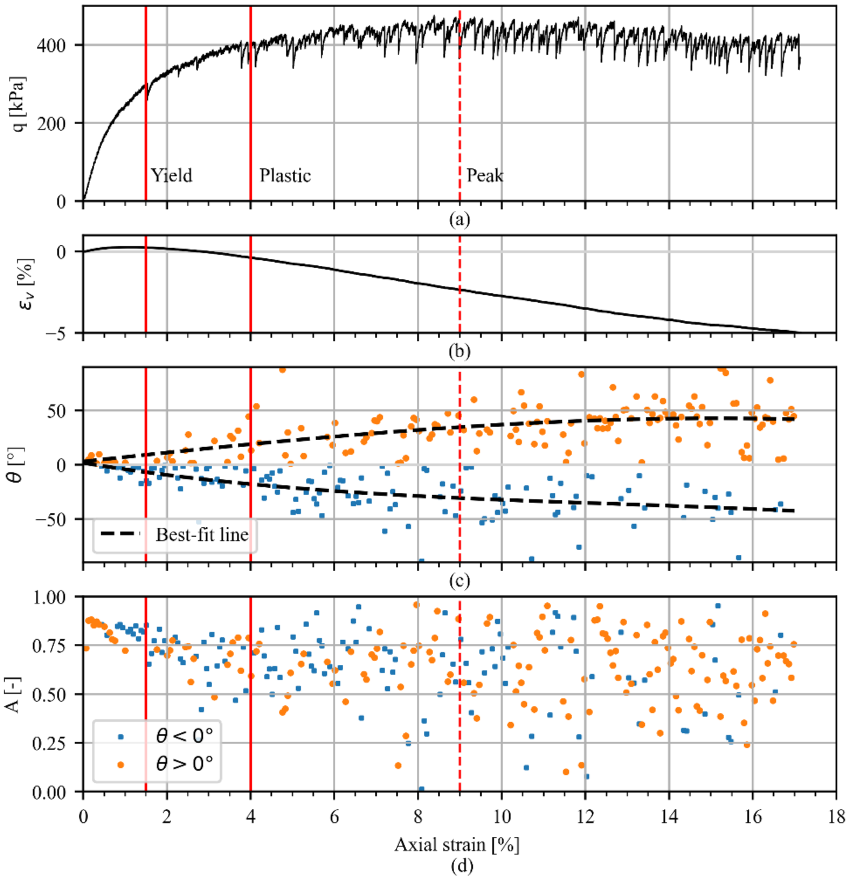

Figure 4. Triaxial test results; (a) deviatoric stress (q), (b) volumetric strain (ε_v) (compression is positive), (c) shear band inclination (θ) and (d) anisotropy of the shear stress distribution (A) with axial strain (ε_A). Note, for θ best fit lines for the two series of conjugated planes is indicated.

After consolidation, the stress in the specimen is isotropic ($A = 0$). During early loading stages the specimen deforms elastically. Thus, the vertical stress in the sample increases while the horizontal stress remains constant. Consequently, the measured anisotropy in the shear strain field is high (e.g. A=0.84 for $\varepsilon_A = 0.5\%$ shown in Figure 3a). In addition, the inclination of the incremental shear strain field is approximately vertical ($\theta \approx 0°$).

Up to 1.5% axial strain the inclination of the major component of the shear strain field remains downward and approximately vertical. In addition, the anisotropy of the strain field remains fairly constant at its maximum value. Thus, ~1.5% axial strain marks a yield condition.

Beyond ~1.5% axial strain the anisotropy of the strain fields decreases with increasing axial strain. This implies that load is not only transferred vertically through the sample, but also laterally across the specimen. The direction of the major component of the strain field starts to deviate from the vertical indicating the presence of strain localization.

At approximately 4% axial strain the measured anisotropy stops decreasing. In addition, at ~4% axial strain the slip stick behaviour, which is associated with plastic deformation, manifests. The rapid oscillations in deviatoric stress results in a corresponding scatter in the measured sample anisotropy. If the axial-strain resolution of the full-field strain fields was low enough to capture the slip-stick behaviour, the scatter might have been reduced.

This behaviour is consistent with that reported by Desrues et al (2007), that found that strain localization coincides with irregularities in the stress-strain curve. Thus, ~4% axial strain marks end of the transition to plastic behaviour. Beyond this axial strain, shear bands can be observed to form in the specimen. Thus, inclinations and anisotropy measured at this stage correspond to those of shear bands, rather than isolated strain localizations.

The models of Coulomb, Roscoe (1970) and Vardoulakis (1980) predict the inclination of the shear band relative to the direction of the major principle stress as 23.3°, 32.9° and 17.0°, respectively. As shown in Figure 4 the inclination of the shear band in this experiment oscillated between approximately -50° and 50° after the peak shear stress has been reached at ~9% strain. Thus, the measured behaviour does not follow any of the three theoretical models. If the shear band formed at the theoretical inclinations of Coulomb or Vardoulakis (1980), it would have had to bisect the platens. However, the lubricated ends are not perfectly frictionless. Consequently, there is still some artificial confinement that forced the shear band to flatten out past the theoretical angle.

The bulging type failure of the sample manifests in the oscillation of the shear band inclination around the vertical axis. Rather than a single shear band forming (which would have been visible as strain softening in the stress-strain curve), shear bands continuously form and dissipate across the sample. First bisecting the sample from the one side, then from the other as the orientation of the weakest plane changes. This behaviour is also illustrated in Figure 3c and d where the shear band at $\varepsilon_A = 3.45 - 3.51\%$ shows a positive inclination ($\theta = +25.7°$) while the shear band at $\varepsilon_A = 4.95 - 5.01\%$ is negative ($\theta = -43.8°$).

The limitation of analysing images captured on a 2D view to study a 3D shear band results in inaccuracies in the anisotropy measurements. When the shear band is perpendicular to the camera the anisotropy is high as the strain localization at the shear band can be observed. However, when the shear band is parallel to the camera the shear strain concentration is not distinct and the anisotropy measured drops far below 0.5. Furthermore, the inclination of the strain concentration is downwards, i.e., the direction of loading. Figure 3h $\varepsilon_A = 10.97 - 11.03\%$ is an example of a shear band that may be developing towards or away from the camera and thus no distinct shear strain concentrations are visible.

Alternatively, the lack of a clearly defined shear band in Figure 3h may coincide with the "stick"-events of the slip-stick behaviour. During the "stick"-events there will be limited shear strain relative to the "slip"-events and no shear band will be visible. A finer axial strain resolution of the DIC measurements is required to further investigate this issue.

5 CONCLUSIONS

Shear band development was successfully quantified in a triaxial specimen prepared using transparent sand, resulting in direct experimental measurement of the inclination of the strain concentrations and the anisotropy of the strain field. The inclination of the strain concentration was derived from the direction of the eigenvector associated with the largest eigenvalue of the image covariance matrix. The anisotropy was defined in terms of the ratio of the magnitude of the two eigenvalues.

Only a single sample was analysed. As such, the specific correlations observed between the shear band inclination and anisotropy and the stress-strain behaviour of the sample cannot be generalized. However, for this specimen in specific, the transition to plastic behaviour was marked by a decrease in the anisotropy of the strain field and the inclination of the strain concentration deviating from 0°. Also, after an initial decrease in the anisotropy and increase in inclination with increasing axial strains, the inclination reach a plateau. At this point, the sample has reached a plastic regime and shear bands can be observed.

Finally, it was found that for this sample the bulging failure mode of the sample manifested as shear bands constantly forming and reforming as quantified by the oscillations in the strain concentration inclination around the vertical axes.

6 ACKNOWLEDGEMENTS

The financial assistance of Tensar International Corporation for this study is acknowledged by the authors. Opinions expressed and conclusions presented are solely those of the authors. The authors are grateful to Mr Etienne Gonzales for the translation of the abstract to French.

7 REFERENCES

Bradski, G. 2000. The OpenCV Library. *Dr. Dobb's Journal of Software Tools*.

Desrues, J., Bésuelle, P., Lewis, H. 2007. Strain localization in geomaterials. *The Relationship between Damage and Localization*, Geological Society, London, Special Publications 289, 47–73.

Dyer, M.R., 1985. *Observations of the stress distribution in crushed glass with applications to soil reinforcement* (PhD). University of Oxford, Oxford.

Ezzein, F.M., Bathurst, R.J. 2011. A Transparent Sand for Geotechnical Laboratory Modeling. *Geotechnical Testing Journal* 36, 590–601.

Galaz, B., Espíndola, D., Melo, F., 2018. Amplification of stick-slip events through lubricated contacts in consolidated granular media. *Physical Review E* 98(4).

Gao, K., Euser, B.J., Rougier, E., Guyer, R.A., Lei, Z., Knight, E.E., Carmeliet, J., Johnson, P.A. 2018. Modeling of Stick-Slip Behavior in Sheared Granular Fault Gouge Using the Combined Finite-Discrete Element Method. *Journal of Geophysical Research: Solid Earth* 123(7), 5774-5792.

Hall, S.A., Bornert, M., Desrues, J., Pannier, Y., Lenoir, N., Viggiani, G., BéSUELLE, P. 2010. Discrete and continuum analysis of localised deformation in sand using X-ray µCT and volumetric digital image correlation. *Géotechnique* 60(5), 315–322.

Hettler, A., Vardoulakis, I. 1984. Behaviour of dry sand tested in a large triaxial apparatus. *Géotechnique* 34(2), 183–198.

Iskander, M., Bathurst, R.J., Omidvar, M. 2015. Past, Present, and Future of Transparent Soils. *Geotechnical Testing Journal* 38(5), 557-573.

Jones, E.M.C., Iadicola, M.A. 2018. *A Good Practice Guide for Digital Image Correlation*. International Digital Image Correlation Society.

Le Bouil, A., Amon, A., Sangleboeuf, J.-C., Orain, H., Bésuelle, P., Viggiani, G., Chasle, P., Crassous, J. 2014. A biaxial apparatus for the study of heterogeneous and intermittent strains in granular materials. *Granular Matter* 16, 1–8.

Marx, D.H., Zornberg, J.G. 2020. Shear band formation in uniformly graded, geotextile reinforced triaxial samples. *Proceedings of the 4th Pan American Conference on Geosynthetics*.

Nguyen, T.B., Amon, A. 2016. Experimental study of shear band formation: bifurcation and localization. *Europhysics Letters* 116(2).

Ozbay, A., Cabalar, A.F., 2016. Effects of triaxial confining pressure and strain rate on stick-slip behavior of a dry granular material. *Granular Matter* 18(3).

Peng, X., Zornberg, J.G. 2019. Evaluation of soil-geogrid interaction using transparent soil with laser illumination. *Geosynthetics International* 26(2), 206–221.

Rechenmacher, A.L., Finno, R.J. 2020. Digital Image Correlation to Evaluate Shear Banding in Dilative Sands. *Geotechnical Testing Journal* 27(1), 13-22.

Roscoe, K.H., 1970. The Influence of Strains in Soil Mechanics. *Géotechnique* 20(2), 129–170.

Schreier, H., Orteu, J.-J., Sutton, M.A. 2009. *Image Correlation for Shape, Motion and Deformation Measurements*. Springer US, Boston, MA.

Scrapelli, G., Wood, D.M. 1982. Experimental observations of shear patterns in direct shear tests, in: *IUTAM Deformation and Failure of Granular Materials Conference*., Balkema, Rotterdam, Delft. 473–483.

Stanier, S.A., Blaber, J., Take, W.A., White, D.J. 2016. Improved image-based deformation measurement for geotechnical applications. *Canadian Geotechnical Journal* 53 (5), 727–739.

Szeliski, R. 2010. *Computer Vision: Algorithms and Applications*. Springer London.

Takano, D., Lenoir, N., Otani, J., Hall, S.A.,2015. Localised deformation in a wide-grained sand under triaxial compression revealed by X-ray tomography and digital image correlation. *Soils and Foundations* 55, 906–915.

Van der Walt, S., Schönberger, J.L., Nunez-Iglesias, J., Boulogne, F., Warner, J.D., Yager, N., Gouillart, E., Yu, T. 2014. scikit-image: image processing in Python. *PeerJ 2*.

Vardoulakis, I. 1980. Shear band inclination and shear modulus of sand in biaxial tests. *International Journal for Numerical and Analytical Methods in Geomechanics*. 4(2), 103–119.

White, D.J., Take, W.A., Bolton, M.D. 2003. Soil deformation measurement using particle image velocimetry (PIV) and photogrammetry. *Géotechnique* 53(7), 619–631.